NUCLEATION OF FAST, INTERMEDIATE AND SLOW SLIP MODES ON THE SAME FAULT

[2,*]K.G. Morozova, [2]V.K. Markov, [2]D.V. Pavlov, [2,3]M.F. Popov & [1,2,*]A.A. Ostapchuk

[1]Moscow Institute of Physics and Technology, Institutsky lane 9, Dolgoprudny, Moscow region, 141700, Russia

[2]Sadovsky Institute for Dynamics of Geospheres of Russian Academy of Sciences, Leninsky av., 38, bldg.1, Moscow, 119334, Russia

[3]Bauman Moscow State Technical University, 2[d] Baumanskaya str., 5, Moscow, 105005, Russia

*Corresponding authors: Alexey A. Ostapchuk (ostapchuk.aa@phystech.edu), Kseniya G. Morozova (morozova@ idg.chph.ras.ru)

The spectrum of slip modes on gouge-filled faults spans a continuum from fast ruptures to slow slip events. The nucleation of a certain slip mode is governed by the frictional heterogeneity of fault interface and the rheological fault stiffness. There is a mounting evidence that a single fault can host multiple slip modes. We present laboratory acoustic emission (AE) experiments on a slider-model. The entire spectrum of fault slip modes with a precise control of mechanical and AE parameters was reproduced and the unity of underlying mechanisms of slip mode nucleation was detected. A comprehensive analysis of AE activity allows revealing coexistence of two distinct subpopulations of acoustic pulses (APs) emitted during a seismic cycle and accompanying nucleation of different fault slip modes. One of them manifests as APs with harsh onsets. The second one exhibits a gradual amplitude rise and a tremor-like waveform. The second AP subpopulation shows longer failure duration and increased energy dissipation. During a seismic cycle, the first AP subpopulation retains parameters of frequency-amplitude distribution, while the second one exhibits a pronounced cyclic recurrence of the *b-value*. The *b-value* of the second subpopulation decreases before slip events and recovers after them. The detected features of AE evolution are common for the entire spectrum of fault slip modes.

Key words: Fractures and faults, Rheology and friction of fault zones, Self-organization, Seismic cycle, Earthquake dynamics.

1. Introduction

The blocky hierarchical structure of the Earth's crust determines its movability and localization of deformations in interblock zones. Faults and large fractures control regularities of accumulation and relaxation of the energy of elastic deformation in a blocky massif (Scholz, 2002; Kocharyan, 2016). The dynamics of relaxation processes that are accompanied by slips along faults is determined by the ratio of the rheological stiffness of the fault to the one of the enclosing massif (Leeman et al., 2016; Kocharyan et al., 2017). Fault slip modes observed in nature span a continuum, given the heterogeneity and complexity of natural systems (Peng, Gomberg, 2010; Burgmann, 2018). Different faults may exhibit just fast slip modes (ordinary earthquakes), or just slow slip modes (low-frequency earthquakes, slow slip events), or even both fast and slow modes together (Veedu, Barbot, 2016; Frank et al., 2016; Ostapchuk et al., 2020).

The frictional instability is the most probable mechanism of the entire continuum of fault slip modes (Schoolz, 2002; Nielsen, 2017). During fault evolution, slip events are triggered when shear stresses reach the ultimate strength at a local fault segment. In the vicinity of the ultimate strength the source stays in a metastable state, so that even a slight fluctuation of stress may lead to a loss of dynamic stability. The transition of a fault to a metastable state is accompanied by a decrease of the shear stiffness of source zone (Johnson, Jia, 2005; Kocharyan, Ostapchuk, 2011). At present measuring ‘in situ’ tectonic stress and fault stiffness is a complex problem. There are several indirect ways to estimate the state of stresses near faults (Rebetsky et al., 2016; Brodsky et al., 2020) and indirect ways to detect manifestations of fault behavior and earthquake nucleation (Frank et al., 2016; Trugman, Ross, 2019). Applying AE technique to passive monitoring of a fault dynamics assumes correlation between the AE activity and the stress-strain state of the fault (Dixon et al., 2018).

The laboratory experiment is a reliable tool to verify new hypotheses and assumptions (Marone, 1998; Rosenau et al., 2017). AE experiments reproduce qualitatively the main statistical laws that describe natural seismicity (Gutenberg-Richter law, Omori law, inverse Omori law) (Lei, 2003; Johnson et al., 2013; Ostapchuk et al., 2019; Lherminier et al., 2019). In laboratory nucleation of slip events is accompanied by variation of scaling properties of AE (Goebel et al., 2013; Riviere et al., 2018), variation of wave propagation velocity (Hedayat et al, 2014; Shreedharan et al., 2021), seismic quiescence (Ostapchuk et al., 2016). The similarity of recurrent fast and slow earthquakes has been demonstrated (Hulbert et al., 2019).

The existing models of seismic activity, describing a certain fault or a source zone, suggest that earthquake nucleation area is an integrated dynamic system which has a specific property of self-organizing criticality (Kuksenko et al., 1996; Turcotte, 1999; De Arcangelis et al., 2016). At the initial stage damage accumulates at the micro-scale. Cracks are uncorrelated and occur randomly. Further evolution of the system lifts the destruction processes to a higher hierarchical level, thus, as the stresses approach the critical value, structural changes spread wider all over the system. Systems spontaneously evolve towards critical states characterized by power laws in the event size distribution. The loss of dynamic stability manifests at the macro-scale as a slip event. The more accurate the earthquake detection technique is, the more distinct is the pattern of large earthquake nucleation (Trugman, Ross, 2019).

This work is devoted to investigation of the acoustic pattern of simulated gouge-filled fault evolution. We explored the entire spectrum of fault slip modes by changing the filler material and revealed acoustic signs of nucleation of fault slip instability. A great number of APs can be detected during a laboratory seismic cycle. Some waveforms resemble classical impulsive earthquakes, while the others are more tectonic tremor-like. Detecting two distinct AP subpopulations and analyzing their scaling characteristics have allowed us to reveal microphysical mechanisms and attribute them to specific acoustic signs of nucleation of different fault slip modes. The findings provide a new insight into predicting the behavior of faults hosting both fast and slow slip modes.

2. Experimental method

Laboratory experiments were performed on a slider-model. A scheme of the set-up is shown in Fig. 1. The model fault – a confined granular layer between two blocks – was subjected to external normal and shear stresses. The moveable granite block (1) 8×8×3 cm^3 in size was put in the middle of the granite base rod 2.5 m long and 10×10 cm^2 in cross section. The contact surfaces of the block and the base rod were made rough by introducing grooves 0.8-1.0 mm deep. The contact gap between the block and the base was filled with a granular material (3). Mixtures of different granular materials were used as fillers. All fillers are listed in the Supplementary Table S1. Their structural properties determined realization of a certain slip mode (Mair et al., 2002; Anthony, Marone, 2005; Kocharyan et al., 2014).

The moveable block slid along the interface under the applied normal and shear forces. The normal force was F_N = 500 N in all the experiments. It was applied by a set of weights. The shear force was applied to the block through an elastic element (6) with the stiffness of K = 55 kN/m. Its free end was pulled at a constant velocity of u_s =8 μm/s. The shear force was controlled with the sensor CFT/5kN (HBM, Germany) (5) accurate to 1 N. The displacement of the block relative to the base was measured with the laser sensor ILD2220-10 (Micro-Epsilon, Germany) (4) in the frequency band of 0-5kHz, with the accuracy of 0.1μm.

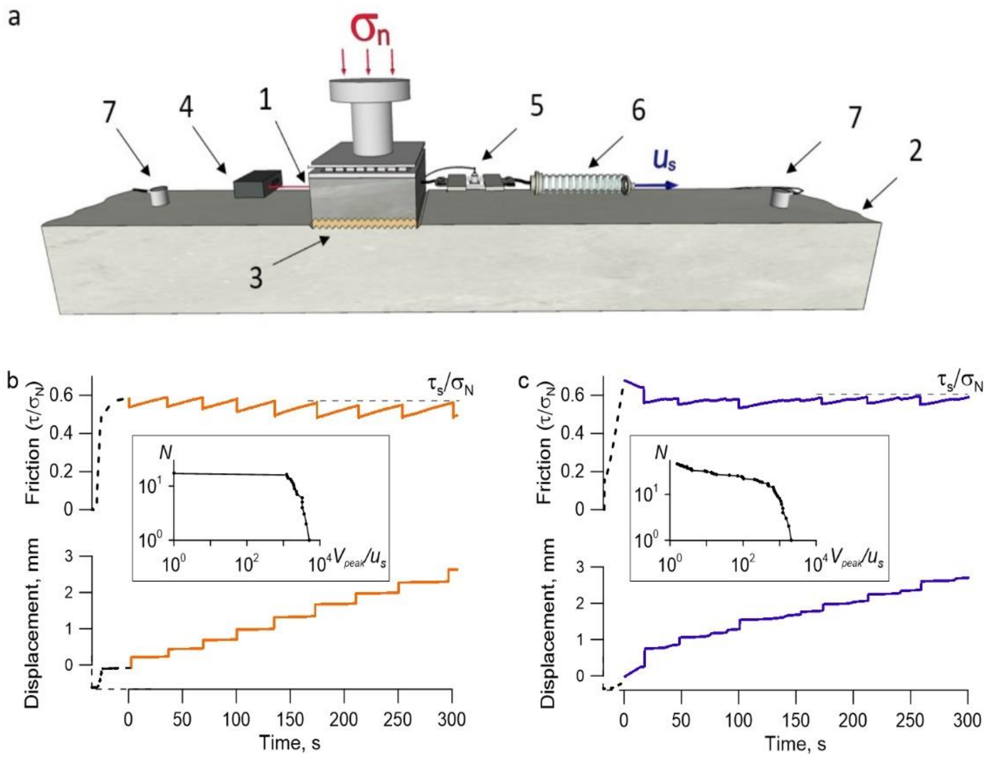

Figure 1. The slider-model performance test.

A scheme of the experimental set-up (a). Mechanical parameters (friction and displacement) and acoustic emission were measured during the experiments.

(1) – moveable block; (2) – base rod; (3) – gouge layer; (4) – laser sensor of displacement; (5) – force sensor; (6) – spring element; (7) – AE sensors.

Characteristic variations of friction and displacement in time for a regular stick-slip (Exp.No 5) (b) and a stochastic sliding regime (Exp. No 23) (c). The point (0,0) corresponds to the moment when the ultimate strength of model fault is reached. We study the 'mature' stage when a regularization of slip behavior has occurred and friction has reached characteristic strength value τ_s. Insets (b, c) show the recurrence plot of slip events (number of slip events with peak velocity more than V_{peak}).

Typical loading curves are presented in Fig. 1b, c. The fault evolution undergoes several stages (Gerasimova et al., 1995; Scuderi et al., 2017). At the initial stage the model fault reaches the ultimate shear strength. Further accumulation of shear deformation leads to the regularization of slip behavior and the contact reaches the new characteristic strength τ_s – the 'mature' stage comes. We consider the 'mature' stage for a detailed analysis. Regularities of a sliding regime are defined by structural, physical and mechanical properties of the filler. Parameters of realized sliding regimes are presented in Supplementary Table S1. Using, for instance, the filler composed of moistened quartz sand with a narrow size distribution of grains, allowed to obtain a regular stick-slip – quasi-periodically repeated fast slip events accompanied by huge drops of friction (Fig. 1b). On the other hand, using the quartz sand with a wide size distribution of grains resulted in a stochastic sliding regime, when the model fault hosted multiple slip modes and slip events were occasional (Fig. 1c). The statistics of realized slip events for regular and stochastic sliding regimes differ.

One of the experimental outputs was the AE accompanying fault evolution. The AE sensors were mounted on the rod at the distances of 0.6 and 0.7m at opposite sides of the moveable block using epoxy agent. The sensors were VS30-V (Vallen System, Germany). The signals were processed by AEP5 charge amplifiers. The operational frequency band was 20–80 kHz (Supplementary Fig. S1). All the AE data were acquired at 1 MHz with the 14-bit analog-to-digital converter E20-10 (L-Card, Russia). The signals were provided in units of voltage.

We used a threshold algorithm for detecting the APs. An AP is identified by the energy flow that exceeds a fixed threshold, according to the following relation:

$$\Pi(t) = \frac{1}{\Delta t}\sum_{t}^{t+\Delta t}\frac{A(t_i)^2}{f_s} \geq 1.5 A_{\min}^2 \tag{1}$$

A(t) is the recorded signal filtered in the frequency band of 20-80 kHz, $A_{\min}^2$ is the variance of the signal. The factor of 1.5 was established in a preliminary analysis so that the AE catalogue would have been as representative as possible. The energy flow was determined in the window Δt=0.5 ms long at steps of $\Delta t/2$. $A_{\min}^2$ was determined in 1 second intervals of AE signals before the shear load started, according to the following relation:

$$A_{\min}^2 = \frac{1}{f_s - 1}\sum_{t_i>0}^{t_i\leq 1}\left| A(t_i) - \frac{1}{f_s}\sum_{t_i>0}^{t_i\leq 1} A(t_i)\right|^2 \tag{2}$$

Figure 2 presents the algorithm of AP detecting. The time t_s when the energy flow starts to exceed the threshold is taken to be the beginning of the AP, and the time t_e when the energy flow went beyond the threshold – the end of the AP. The points of onset and termination were determined with the accuracy of 250 μs. The AP spectra differed essentially. Some APs showed maximum at the frequency of 40-70 kHz, while the others - at about 20 kHz.

We verified by visual inspection that every recorded AP was captured. Random choice of 1000 APs showed that only 47 multi-pulses were misidentificated as simple pulses.

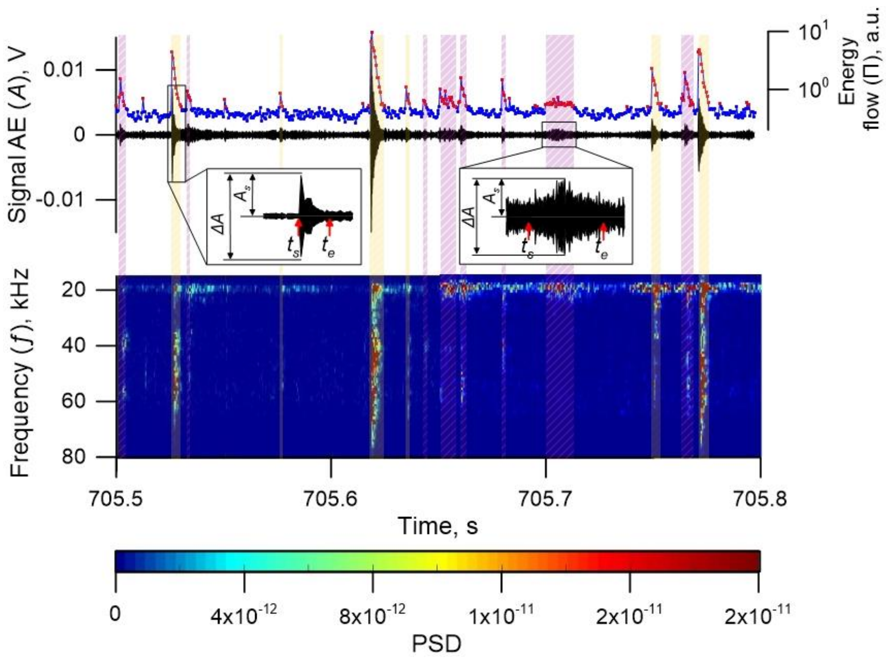

Figure 2. Algorithm of AP detection (Exp. No 5).

First, AE signal was filtered in the frequency range of 20-80 kHz with a Butterworth filter. Then, the energy flow (Π) was calculated (blue line). Red dots designate the excesses over a fixed experimental threshold determined by relation (1). AE signals identificated as APs are marked with dashed areas. The spectrogram of AE signal clearly shows the identificated APs. Insets show parameters of APs: onset (t_s), termination (t_e), amplitude (A_s) and peak-to-peak amplitude (ΔA)

The following parameters were retrieved from the detected APs: duration (dt), amplitude (A_s), peak-to-peak amplitude (ΔA) and energy (E), which was estimated as follows:

$$E = \Delta t \sum_{t_s}^{t_e} A^2(t_i) \,. \tag{3}$$

We obtained amplitudes only from the digital waveforms and performed energy estimations by time integration of signals in volts. So these energy estimations were presented in non-physical energy units.

Assuming the self-similarity of the earthquake process, which consequently implies a power-law distribution, we checked the AE catalogue. In order to compile a homogeneous and complete AE catalogue with respect to duration and amplitude we eliminated APs with durations less than 1.5 ms and amplitudes lower than 60 dB.

It seems likely that the waveform of an AP points to the mechanism and intensity of the evolution process inside the fault (Shiotani et al., 2001; Zigone et al., 2011; Ostapchuk et al., 2016). In order to characterize both the stage of AP rise and the stage of decrease, we have introduced the waveform index *WI*. The *WI*-value was calculated through the formula:

$$WI = \frac{(t_{\mathrm{max}} - t_{\mathrm{s}})}{(t_{\mathrm{e}} - t_{\mathrm{max}})}, \tag{4}$$

t_{max} is the time when the maximum peak-to-peak amplitude was reached.

APs of different waveforms and amplitudes were emitted in fault sliding. Depending on the realized sliding regime the rate of APs varied from single "clicks" at intervals of several seconds to regularly repeating APs at intervals of 1-2 ms. Among all the recorded APs it was necessary to distinguish those emitted during slip events and at the stage of slip event preparation (Fig. 3).

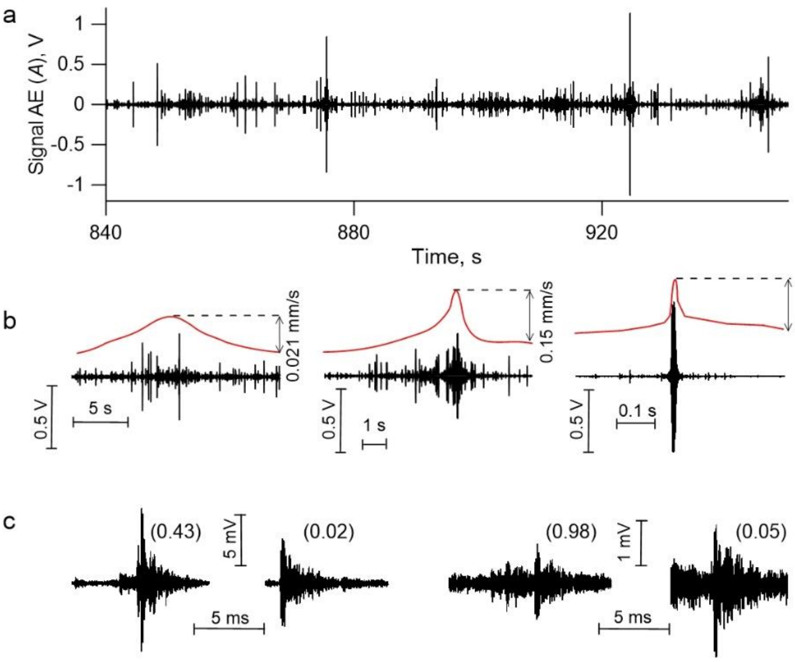

Figure 3. AE data.

The AE signal recorded during fault sliding (Exp. No 13) (a). 'Coseismic' APs corresponding to slip events (b) and 'interseismic' APs corresponding to slip event preparation (c). In Fig. 3b red line corresponds to variations of block velocity with time. In Fig.3c the *WI*-value is indicated in parentheses.

Introduction of the *WI* parameter was dictated by the necessity to take into consideration various processes of self-organization taking place in a stressed granular medium in the course of formation of inhomogeneous stressed conditions in a gouge-filled fault during sliding (Hadda et al., 2015; Gao et al., 2019). In the case of rock failure, the *WI*-value bases on two important aspects, provided that detected are AE waves that directly reflect a source-time function (Shiotani et al., 2001; Besedina et al., 2020). First, the gradient of the ascending part of the waveform becomes smaller as fracture propagates; second, low-frequency components of the waveform should become dominant as the fracture progresses (Shiotani et al., 2001).

It is worth mentioning that more than 95 % of detected APs had *WI*-values within the range of 0 to 1. The relative error of *WI*-value determination was less than 0.15. The APs with the values of *WI* >> 1 were treated as double- or multi-pulses. They were not considered in our analysis.

3. Results

3.1. Continuum of fault slip modes

Using mixtures of different materials, we managed to reproduce in laboratory the entire spectrum of slip modes. Mechanical parameters of realized slip events vary in a wide range (Fig. 4a, b). Parameters of slip events form a connected set in the space (V_{peak}, T, ΔL). Considering different parameters lets us to qualitatively separate the events into three modes. The first mode is the fast slip events with peak velocity above 8 mm/s (1000 u_s) (fig., 3b) and duration less than 0.8 s. The fastest slip events had peak velocities up to 48 mm/s (6000u_s) and the relative value of friction drop down to 0.1. Single high-amplitude APs with durations corresponding to the ones of slip events were emitted in fast modes. The second mode is the slow slip events. Slow slip events had peak velocities of 2-5 u_s and relative changes of friction less than 10^{-2}. The slow slip events were accompanied by emission of cascades of APs that resembled the low frequency earthquake bursts during slow slip events (SSEs) in nature (Fig. 3b) (Frank et al, 2016). Duration of laboratory slow slip events varied from 2s to 15-20s. It should be noted that slow slip events with durations exceeding 10 s were specific for the model fault with clay-rich gouge. The third mode is the intermediate slip events. It shows a high variety of parameters and demonstrates the diversity of realized slip events. The third mode fills in the gap between slow and fast slip events, indicating a continuum of slip modes.

The ensemble of realized slip events demonstrates high spread of the emitted AE energy. The AE energy differs by more than 2 orders of magnitude for slip events with equal "seismic moments" (Supplementary Section S1). Considering the data of a single experiment, an increase in the seismic moment is accompanied by a power-law increase in the emitted AE energy (fig.4c, inset). Unfortunately, it is impossible to detect an analogous regularity considering the complete ensemble of realized slip events. The reason is the alteration of the structure of the model fault filler. The filler composition controls the radiation efficiency of slip events (Kocharyan et al., 2017). Hence, events with equal seismic moments can show different values of emitted energy on faults with different filler composition.

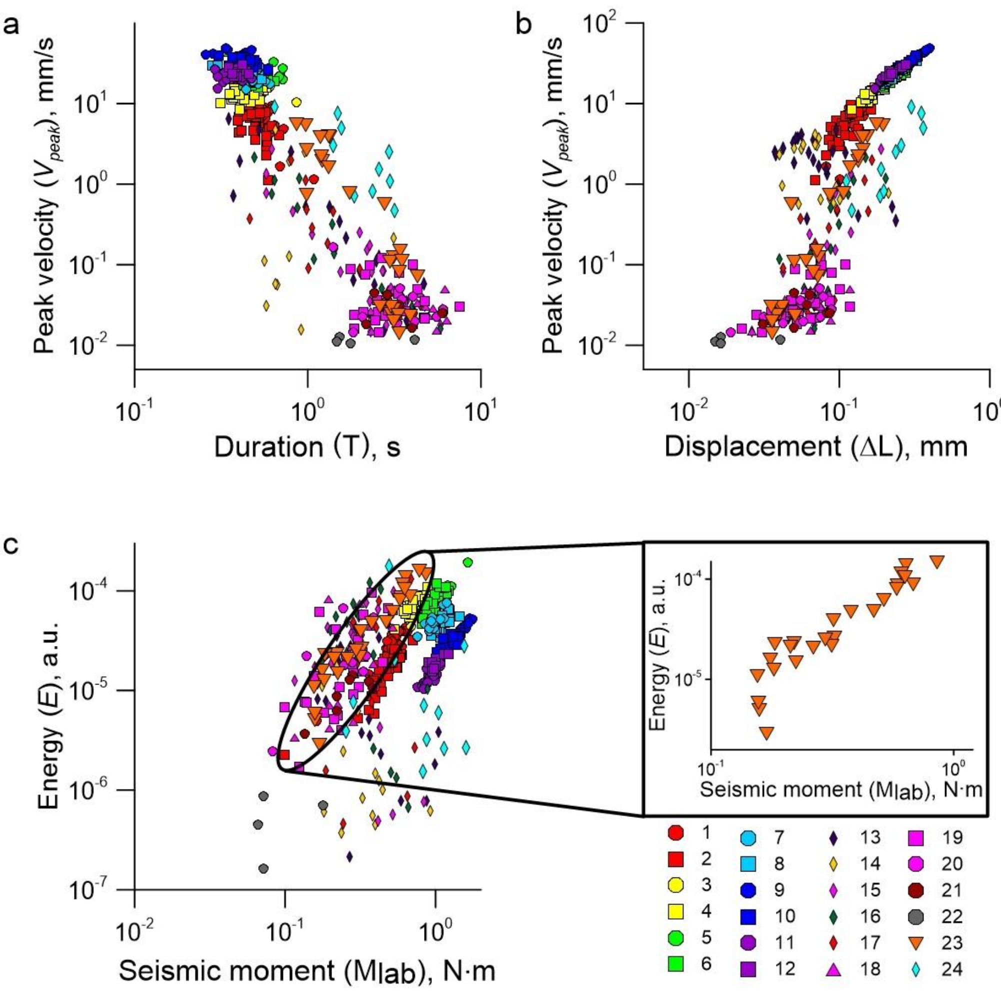

Figure 4. Variations of slip event parameters.

Peak velocity dependences on slip duration (a) and cumulative slip (b) show that the ensemble of realized slip events form a connected set in the space (cumulative slip (ΔL), peak velocity (V_{peak}), slip duration (T)).

Comparison of the laboratory 'seismic' moment and the AE energy of 'coseismic' APs (c). Inset shows the data of Exp. No 23, the exponent is 1.8±0.1. The laboratory seismic moment is $M_{lab} = K \cdot \Delta L \cdot s$ (where K and s are spring stiffness and block length, respectively).

The symbols 1-24 correspond to experiments listed in the Supplementary Table S1.

The experiments testify that the entire spectrum of sliding regimes results from the frictional instability of the model fault, just at the expense of friction. Though we do not exclude other mechanisms that may lead to formation of different slip modes, such as variations of fluid pore pressure, dehydration reactions, brittle-ductile transition and others (Reber et al., 2015; Saffer, Wallace, 2015; Cruz-Atienza et al., 2018; Burgmann, 2018).

3.2. Two AP subpopulations

The change of stress-strain conditions of the model fault results in various structural changes and is accompanied by a great number of APs. In general, the amplitude-frequency distribution of APs is a superposition of a power-law distribution in the low-amplitude range and a peak-like distribution in the high-amplitude range (Fig. 5a).

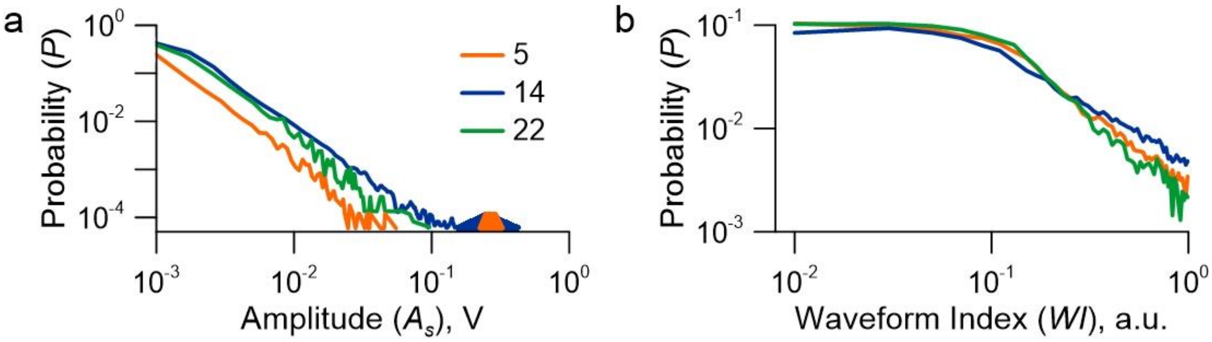

Figure 5. Probability density functions of APs.

AP statistics demonstrates an essential difference between amplitude-frequency (a) and waveform-frequency (b) distributions. The 'coseismic' APs corresponding to slip events form the separate high-amplitude peak, which is marked by the filled area. The waveform index plot allows to detect the characteristic (cut-off) value (*WI*=0.1). Numbers correspond to experiments listed in Supplementary Table S1.

In the range of low A_s values the AP statistics is approximated with high accuracy by the power-law:

$$\lg(N) = a - b\lg\left(\frac{A_s}{A_0}\right) \tag{5}$$

where N is the number of pulses with amplitudes of A_s. The value lg (A_s/A_0) corresponds to AE body-wave magnitude (Lei, 2003), a and b are two positive constants. The *a-value* is a measure of AP activity, which depends on the time window of observations. The slope of recurrence plot (*b-value*) is a scaling parameter, which characterizes the process of self-organization of the medium (Gutenberg, Richter, 1944; Turcotte, 1999). The power law behavior is also typical for the AP distributions over energy (*E*) and duration (*dt*).

The distribution of APs over the *WI* parameter shows two specific domains (Fig. 5b). This can be written as follows:

$$N = \begin{cases} a_{WI}, WI \le 0.1 \\ c_{WI} \cdot WI^{-w}, WI > 0.1 \end{cases}, \qquad (6)$$

where N is the number of pulses whose waveform parameters equals WI, a_{WI} and c_{WI} are positive constants, which are determined by the intensity of AE. There is also the cut-off value of WI=0.1. Persistence of the cut-off value in all the performed experiments, probably, points to spatial peculiarities of the internal self-organization of the medium – formation of grain clusters of limited size (Hadda et al., 2015). So, grain clusters that emitted APs with WI≤0.1 had approximately equal sizes, while grain clusters that emitted APs with WI>0.1 showed size variation. The index *w-value* characterizes the non-uniformity of AP ensemble over the *WI* parameter, while its alteration probably points to the predominant mechanism of AP generation. One can see in Fig.2 that pulses with harsh onsets (WI≤0.1) have spectral maxima at the frequencies of 40-70 kHz, while tremor-like signals demonstrate an essential spectral increase in the vicinity of 20 kHz.

The essential difference of the AP distributions over amplitude and over waveform index points to the necessity to consider the *WI* parameter as an independent characteristics of the process of fault evolution. The presence of a characteristic cut-off point in the waveform-frequency distribution motivates to conduct a clusterization of the ensemble of detected APs over the *WI*-value. APs with *WI*≤0.1 will compose mode I. They manifest as wave trains with harsh onsets. Mode II will include APs with *WI*>0.1. They exhibit gradual amplitude rises and tremor-like waveforms.

To better understand the physical mechanism of internal processes of self-organization, let us consider the scaling relationships for the mode I and mode II of APs. The scaling relationships provide important insights into and constraints on the dynamics of internal processes. Fig. 6 shows log-log trends between different AP parameters. Such a presentation gives an opportunity to compare them to scaling laws for ordinary ‘fast’ earthquakes and SSEs (Peng, Gomberg, 2010; Nishitsuji, Mori, 2014).

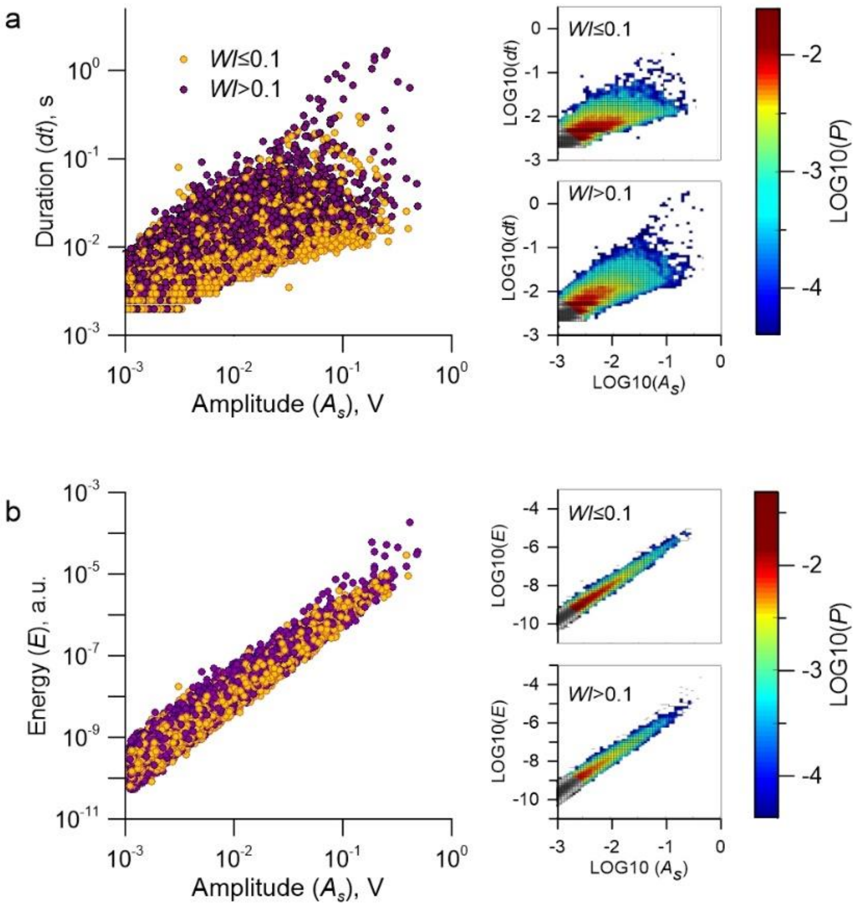

Figure 6. Scaling of two AP subpopulations in Exp. No 13.

(a) Duration versus amplitude of AP (mode I – yellow, mode II – purple). The complete set of APs is limited by two solid lines given by relations (7). Right plots show the two-dimensional probability density functions of the AP mode I (upper) and the AP mode II (lower).

(b) Energy versus amplitude of AP. The energy varies by more than an order of magnitude for APs with one and the same amplitude. Right plots show the two-dimensional probability density functions of the AP mode I (upper) and the AP mode II (lower).

The event duration scaling is viewed as a key to unraveling the rupture mechanism in nature and lab. All the recorded APs form a connected set, which is limited by two boundaries:

$$dt_{upper} \sim A_s^{1.2\pm0.2}$$
$$dt_{bottom} \sim A_s^{0.5\pm0.1} \quad . \qquad (7)$$

In nature this may correspond to the scaling between the seismic moment and the duration ranging from $T \sim M_0^{0.8\pm0.1}$ to $T \sim M_0^{0.3\pm0.1}$ (see Supplementary Section S2). At the same time one can see that AP mode I localizes closer to the lower boundary, than AP mode II. It means that for APs of equal amplitudes to be realized, mode II should have a longer failure duration than mode I. Moreover, for the AP mode I a slower growth of radiated energy with scale is observed, than for the AP mode II (Fig. 4b, Supplementary Fig. S2). Hence, the mode II exhibits an increased energy dissipation at the micro-scale.

To understand the fundamental differences between the detected AP modes, it will be appropriate to consider the model fault as a complex two-component dynamic system. Fig. 7 shows variations of mechanical and acoustic parameters for regular and stochastic sliding regimes. In order to investigate the temporal evolution of the *b-value*, we calculated *b-values* using the method of least squares in a running window for an equal number of APs (nn = 100) with a running step of nn/2 (50 % overlap).

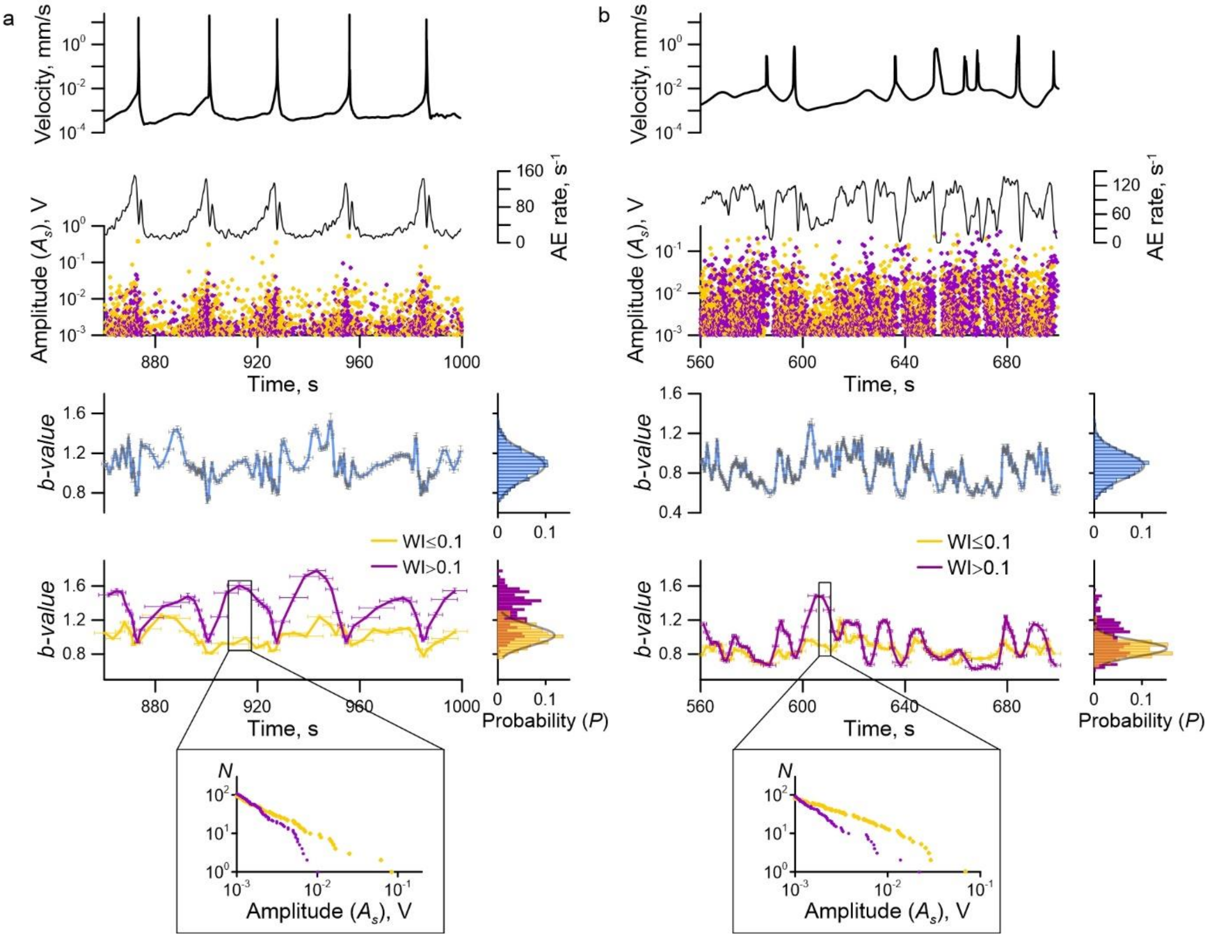

Figure 7. Evolution of model fault state.

Variations of sliding velocity and AP parameters for a regular stick-slip (Exp. No 3) (a) and a stochastic sliding regime (Exp. No 13) (b). Insets show APs distribution in a running window for mode I (yellow) and mode II (purple).

Unlike the stochastic regime, the regular regime shows a high correlation between the sliding velocity and the AE rate. Occasional variations of *b-value* are observed for both regular and stochastic regimes for the complete population of APs. Histograms of *b-value* obey the normal distribution law.

Separation of APs into two subpopulations shows an essential difference of time variations of *b-value*. Occasional alterations are observed for the AP mode I (*WI*≤0.1), while the AP mode II (*WI*>0.1) shows systematic variations. Inset shows recurrence plot of APs for two distinct subpopulations.

A stable repeated pattern of variations of both mechanical and AE parameters is observed during a regular stick-slip. Variations of block sliding velocity and AE rate testify three typical stages of a seismic cycle. After the dynamic failure, the post-seismic stage comes with a decreasing velocity of block sliding and AE rate. The lowering activity is described by the law of Omori-

Utsu (Lherminier et al., 2019; Ostapchuk et al., 2019). Then approximately stable minimal values of velocity and AE rate persist at the inter-seismic stage. As the system approaches the slip event, an accelerated block sliding starts accompanied by an increase of AE rate. At the final part of inter-seismic stage leading to failure, statistics of APs can be described by the inverse Omori's law (Ostapchuk et al., 2019; Johnson et al., 2013). No clear staging of a seismic cycle is observed when analyzing variations of the *b-value* of the complete population of APs. The *b-value* distribution obeys the normal law. It should be noted that the cyclicity of *b-value* for the complete population of APs in a limited range of amplitudes has been mentioned in a few works (Reviere et al., 2018; Lei et al., 2018). Clusterization of APs into two subpopulations eliminates the ambiguity of the pattern of *b-value* variations. For a regular stick-slip the analysis of *b-value* histograms shows that the AP mode I ($WI \leq 0.1$) exhibits an almost constant *b-value* and time variations are occasional (histogram obeys the normal distribution). At the same time the AP mode II demonstrates certain periodic variations of *b-value*, and the histogram cannot be approximated by a normal distribution. If we look at the laboratory seismic cycle just after a dynamic failure at the first stage of fault recovery, we can see that a fast growth of *b-value* occurs. Then the stage of creep comes at a minimal velocity, and *b-value* remains almost constant, which in the presented case manifests as a peak in the *b-value* histogram around the value of 1.4. At the final stage, a monotonic decrease of *b-value* is observed, which means that the share of high-amplitude APs of mode II grows.

In a stochastic regime the pattern of parameter alteration is much more complicated. It seems impossible to detect stages of the cycle through AE rate and block sliding velocity. Small relative variations of AE rate are observed before slip events, while abrupt drops occur only after the fastest slip events. There are no unambiguous variations of *b-value* over the complete AP population. However, if one performs clusterization of APs, the two-mode population becomes apparent, and the staging of fault evolution manifests clearly (Fig. 7b). The AP mode I has only a single specific *b-value* during shear, and variations are random. A more pronounced variation is observed if compared to the regular stick-slip. This probably results from the peculiarities of self-organization when fast and slow slip events take turns. The AP mode II shows staging of *b-value* alteration. The *b-value* decreases before each of the slip events and recovers after them.

So, we can say that two AP subpopulations are emitted during gouge-filled fault sliding. These subpopulations have different scaling characteristics and different peculiarities of evolution. The obtained results indirectly indicate that at the meso-scale a gouge-filled fault should be treated as a two-component dynamic system. One of the sub-systems exhibits scaling invariance in time, and structural changes are accompanied by APs with harsh onsets (mode I). The other sub-system demonstrates periodical variations of scaling parameters in time, and the transition to the critical state is accompanied by an increase of the specific scale of structural alterations. The evolution of the second subsystem is accompanied by APs with a gradual amplitude rise (mode II), which have longer failure durations and exhibit an increased energy dissipation.

4. Discussion

The obtained results improve our understanding the nucleation of fast, intermediate and slow slip events on faults at the micro-level. Nucleation of slip events is accompanied by changes of fault stress state and emission of APs with different waveforms. It should be noted that laboratory experiments are by no means a sort of scale modeling since it is simply impossible to fulfill all the similarity criteria in this case (Rosenau et al., 2017). Results of laboratory experiments should be considered as insights into fundamental properties of geomaterials and their structural peculiarities which determine fault slip behavior.

Most scholars consider the regular stick-slip, when slip events take place quasi-periodically, as the dominant fault sliding regime. However, there are very few known faults with regular periodicity of characteristic earthquakes at the human timescale (Ben-Zion, 2008). Meanwhile, evidence appears systematically, that a single fault hosts both fast and slow slips (Ito et al., 2013; Meng et al., 2015; Villegas-Lanza et al., 2016). So, we believe that the stochastic sliding regime with aperiodic slip events is widespread in nature and a single fault can host multiple slip modes.

Improving methods of seismic signal processing point to an ambiguity in SSE scaling. Recent observations in different fault zones suggest that SSEs follow the same moment duration scaling as earthquakes, unlike qualitatively different scaling proposed by earlier studies (Peng, Gomberg, 2010; Michel, et al., 2019; Frank, Brodsky, 2020). For example, the Cascadia slow slip events manifest a cubic moment-duration scaling and can produce pulse-like ruptures similar to fast slip events (Michel, et al., 2019). Numerical simulations urge the same frictional origin for both earthquakes and SSEs and show that both simulated and natural SSEs have rupture velocities and stress drops that increase with event magnitudes (Dal Zilio et al., 2020).

The spectrum of slip behaviors is governed by frictional dynamics via the interaction of the contact frictional properties, the effective normal stress, and the elastic stiffness of the surrounding material (Leeman et al., 2016; Barbot, 2019; Ostapchuk et al., 2020). The evolution of the model gouge-filled fault is controlled by peculiarities of formation and destruction of conglomerates of loaded grains at the meso-scale, the so called ‘force chains’ (Mair et al., 2002; Hayman et al., 2011; Lherminier et al., 2019). The assembly of these chains has a certain spatial structure and a relatively low specific weight inside the medium (Gao et al., 2019). Thus, two structural subsystems emerge inside a stressed fault – a consolidated force skeleton and rather moveable relatively unloaded areas (Gao et al., 2019). We had no chance to visualize the inner processes of self-organization in the performed experiments, but we believe that the detected regularities of alteration of AP ensemble do result from the evolution of the two structural subsystems. Probably, the change of stressed force skeleton is accompanied by emission of the AP mode I, while the dynamics of unloaded areas – by AP mode II. When the force chains (loaded grain conglomerates with limited sizes) are destroyed, the high-frequency AE waveforms with harsh onsets are emitted (Hadda et al., 2015; Gao et al., 2019). At the same time in the unloaded areas the relative decrease of stresses, acting on grains, leads to a decrease of the characteristic frequency of the AE waveforms generated by those conglomerates (Michlmayr, Or, 2014). It is seen in Fig.2 quite distinctly that the tremor-like signal produces the spectral maximum in the vicinity of 20 kHz.

Improving the techniques of detecting weak earthquakes and their statistical analysis allows to obtain important information about fault dynamics and to trace the nucleation of large earthquake (Trugman, Ross, 2019; Gulia, Wiemer, 2019). In our experiments detecting the two subpopulations of APs can form a new basis for determining the critical state of slip event nucleation. We have formulated a simple criterion of an "alarm". It is based on tracing specific acoustic manifestations of fault evolution in time - "If for the AP mode II for three successively estimated *b-values* a monotonic decrease is observed $b(t_{i-2}) > b(t_{i-1}) > b(t_i)$, then the alarm starts at the time t_i. The end of the alarm is the time when the slip event starts (the "true" alarm), or the time t_n, when an increase of *b-value* is observed again $b(t_{n-1}) < b(t_n)$ (the "false" alarm) (Fig. 8, the inset). Fig. 8 presents variations of *b-value* in time for the AP mode II and "the raise of alarm" when the transition of the fault to the critical state starts.

During a regular stick-slip (Fig. 8a) the duration of the alarm was 3.9±1.9s, while the recurrent time of dynamic failures was 34.2±0.8s. The alarm covers the whole pre-seismic stage of the seismic cycle. At the same time, it is important to note that the critical stage (when an event can be triggered by a weak disturbance) emerges at stresses close to the critical ones at the end of the pre-seismic stage (Kocharyan et al., 2018). For the stochastic regime (Fig. 8b) the pattern of *b-value* alteration is more complex, but the chosen alarm criterion is sensitive for such a regime too. A decrease of *b-value* signifies both the forthcoming fast and slow slip events, but more complex mechanisms of self-organization lead to "false alarms" (Ren et al., 2019) (Fig.8b, the inset).

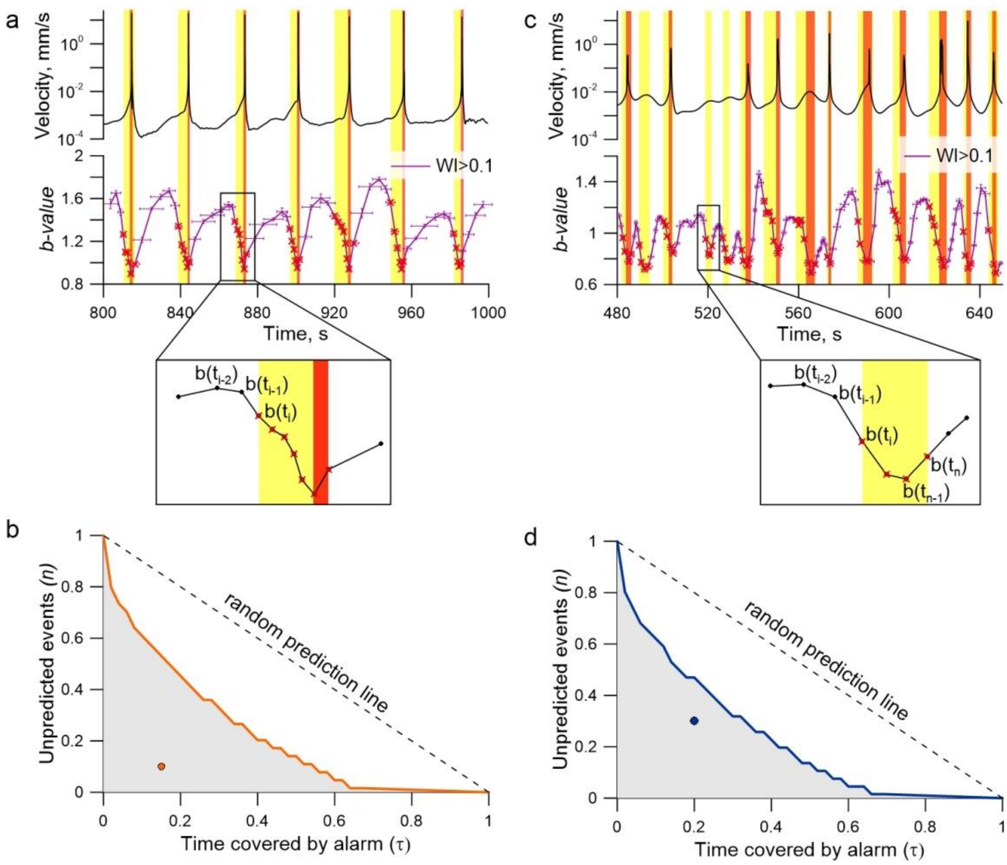

Figure 8. Transition of the model fault to a critical state.

Variations of block velocity and *b*-value of the AP mode II for a regular stick-slip in Exp. No 4 (a) and a stochastic sliding regime in Exp. No 13 (b). The yellow areas correspond to alarm intervals, the red ones – to slip events. Insets show algorithms of the "true" alarm (a) and the "false" alarm (c).

We use the Molchan's diagram to evaluate the predictive power for regular (c) and stochastic (d) sliding regimes. Shaded circles show the performance of prediction algorithm. Random binomial predictions occupy the diagonal. Random predictions with fixed alarm time (τ) fall in the grey area with the probability of $\alpha=10^{-5}$.

The established criterion of the transition of a fault to the critical state should be considered as a step to understanding the basic earthquake nucleation mechanism and to improve the estimation of seismic hazard. The Molchan's error diagram is used to evaluate the predictive power of our prediction algorithm and its stability (Molchan, 2003; Molchan, 2010). We use two interdependent measures of prediction quality: the fraction of unpredicted events ν, and the fraction of alarms τ. Each prediction corresponds to a single point in (τ, ν) space. The error diagram for our prediction of the transition of the fault to the critical state of seismic cycle is presented in Fig. 8c,d. The τ-axis corresponds to the relative alarm time, the ν-axis – to the share of missed slip events. An extremely simple but easily tractable model of prediction which produces alarms independent of the target earthquakes is the random binomial prediction (Molchan, 2003; Shebalin et al., 2006). The probability for a random binomial prediction with a given value of τ to fall within the shaded area is less than or equal to 10^{-5} (0.001 %). The point corresponds to our prediction algorithm indicating high predictive power both for the regular and the stochastic sliding regimes. The efficiency of the precursor J_m is defined as:

$$J_m = 1 - \nu - \tau, \quad (8)$$

The value of J_m lies in the range of (0…1). The nearer the value to 1 is, the more reliable is the raise of alarm. In our experiments the efficiency of the method for a regular stick-slip is $J_m = 0.59…0.83$, while for the stochastic sliding regime that includes both fast and slow slip modes the value is $J_m = 0.4…0.65$ (Supplementary Table S1). For comparison, the efficiency of the ETAS forecasting model for earthquakes M>6 in Southern California is 0.29 (Lippiello et al., 2012). Predictions based on the ultralow frequency magnetic data show the efficiency of about 0.23 (Han et al., 2017). The forecasting technique based on the effect of modulation of high frequency seismic noise in Kamchatka gives the value of about 0.5 for target earthquakes M≥6 (Saltykov, 2017). Thus, the prediction criterion based on detecting the two AP subpopulations turns to be highly effective both for fast, intermediate and slow slip events. The introduced alarm algorithm actually indicates that the fault slip is imminent, but the precise temporal imminence is not defined. The temporal imminence is defined randomly to a great extent, because at the critical stage even a weak disturbance can trigger an event (Kocharyan et al., 2018).

5. Conclusions

A unified pattern of fault slip behavior evolution is a fundamental issue. It requires linking seismic, mechanical and structural data. In the present study, we have revealed two distinct subpopulations of APs, which reflects the complexity of internal fault structure at the meso-scale. Different scaling is intrinsic to those subpopulations. The two subpopulations differ in failure duration and energy dissipation. At the macro-scale we observed a similar mechanical and AE pattern of nucleation of fast, intermediate, and slow slip modes on a model fault. This allows us to speak about the unity of physical mechanisms of nucleation of the entire spectrum of fault slip modes. Revealing the two AP subpopulations and tracing theirs scaling parameters allows us to introduce a new short-term precursor of fault slip, which may improve the seismic hazard assessment.

Acknowledgements

This work was partially supported by RFBR and NSFC according to the research project No. 20-55-53031 for K.G.Morozova, D.V.Pavlov & A.A.Ostapchuk. V.K.Markov & M.F.Popov acknowledge Program No. AAAA-A17-117 112350020-9 of The Ministry of Science and Higher Education of the Russian Federation.

Data availability. All the data that support findings of this work were collected on geomechanical test bench of the Sadovsky Institute for Dynamics of Geospheres of Russian Academy of Sciences. All data sets used in this paper are available on Mendeley Data (doi: 10.17632/kykwmjmpgf.2)

References

Anthony, J.L., Marone, C., 2005. Influence of particle characteristics on granular friction. J. Geophys. Res. 110, B08409. https://doi.org/10.1029/2004JB003399.

Barbot, S., 2019. Slow-slip, slow earthquakes, period-two cycles, full and partial ruptures, and deterministic chaos in a single asperity fault. Tectonophysics. 768, 228171. https://doi.org/10.1016/j.tecto.2019.228171

Ben-Zion, Y., 2008. Collective behavior of earthquakes and faults: Continuum–discrete transitions, progressive evolutionary changes, and different dynamic regimes. Reviews of Geophysics 46, 1–70. doi: 10.1029/2008RG000260.

Besedina, A.N., Kishkina S.B., Kocharyan, G.G., et al. 2020. Weak induced seismicity in the Korobkov iron ore field of the Kursk magnetic anomaly. Journal of Mining Science 56, 339-350, https://doi.org/10.1134/S1062739120036818.

Brodsky, E.E., Mori, J.J., Anderson, L., et. al. 2020. The state of stress on the fault before, during, and after a major earthquake. Annual Review of Earth and Planetary Sciences 48 (1), 49-74.

Burgmann, R., 2018. The geophysics, geology and mechanics of slow fault slip // Earth and Planetary Science Letters 495, 112–134. https://doi.org/10.1016/j.epsl.2018.04.062.

Cicerone, R.D., Ebel, J.E. & Britton, J.A., 2009. A systematic compilation of earthquake precursors. Tectonophysics 476, 371-396. https://doi.org/10.1016/j.tecto.2009.06.008

Cruz-Atienza, V.M., Villafuerte, C., Bhat, H.S., 2018. Rapid tremor migration and pore-pressure waves in subduction zones. Nat.Commun 9, 2900. https://doi.org/10.1038/s41467-018-05150-3.

Dal Zilio, L, Lapusta, N., Avouac, J.-P., 2020. Unraveling scaling properties of slow-slip events. Geophysical Research Letters 47 (10). https://doi.org/10.1029/2020GL087477

de Arcangelis, L., Cataldo Godano, C., Grasso, J.R., Lippiello, E., 2016. Statistical physics approach to earthquake occurrence and forecasting. Physics Reports, 628, 1-91. https://doi.org/10.1016/j.physrep.2016.03.002.

Dixon, N., Smith, A., Flint, J.A., et al. 2018. An acoustic emission landslide early warning system for communities in low-income and middle-income countries. Landslides 15, 1631–1644. https://doi.org/10.1007/s10346-018-0977-1

Frank, W., Shapiro, N.M., Husker, A., Kostoglodov, V., Gusev, A.A., & Campillo, M., 2016. The evolving interaction of lowfrequency earthquakes during transient slip. Science Advances, 2(4), e1501616. https://doi.org/10.1126/sciadv.1501616.

Gao, K., et al., 2019. From stress chains to acoustic emission. Phys. Rev. Lett. 123, 048003, doi: 10.1103/PhysRevLett.123.048003.

Gerasimova, T.I., Kondratev, V.N. & Kocharyan, G.G., 1995. Modeling features of shear deformation of fissures containing filler. Journal of Mining Science 31 (4), 288-295, doi: 10.1007/BF02048229.

Goebel, T.H.W., Schorlemmer, D., Becker, T. W., et al., 2013. Acoustic emissions document stress changes over many seismic cycles in stick-slip experiments. Geophysical Research Letters 40, 2049-2054. https://doi.org/10.1002/grl.50507

Gulia, L., Wiemer, S. 2019. Real-time discrimination of earthquake foreshocks and aftershocks. Nature 574, 193–199. https://doi.org/10.1038/s41586-019-1606-4

Gutenberg, B., Richter, C. F. 1944. Frequency of earthquakes in California. Bull. Seismol. Soc. Am. 34, 185–188.

Hadda, N., Nicot, F., Wan, R., Darve, F., 2015. Microstructural self-organization in granular materials during failure. Comptes Rendus Mecanique 343 (2), 143-154. https://doi.org/10.1016/j.crme.2014.09.009

Hayman, N.W., et al., 2011. Granular controls on periodicity of stick-slip events: kinematics and force-chains in an experimental fault. Pure Appl. Geophys. **168**, 2239. doi: 10.1007/s00024-011-0269-3.

Hedayat, A., Pyrak-Nolte, L. J. & Bobet, A., 2014. Precursors to the shear failure of rock discontinuities. Geophys. Res. Lett. 41, 5467–5475, https://doi.org/10.1002/2014GL060848

Hulbert, C., Rouet-Leduc, B., Johnson, P.A. et al. 2019. Similarity of fast and slow earthquakes illuminated by machine learning. Nature Geosci 12, 69–74. https://doi.org/10.1038/s41561-018-0272-8.

Ito, Y., Hino, R., Kido, M., et al., 2013. Episodic slow slip events in the Japan subduction zone before the 2011 Tohoku-Oki earthquake. Tectonophysics 600, 14-26. https://doi.org/10.1016/j.tecto.2012.08.022

Johnson, P.A., Ferdowsi, B., Kaproth, B.M. et al. 2013. Acoustic emission and microslip precursors to stick-slip failure in sheared granular material. Geophysical Research Letters 40, 1-5, doi: 10.1002/2013GL057848.

Johnson, P., Jia, X. 2005. Nonlinear dynamics, granular media and dynamic earthquake triggering. Nature 437, 871–874. https://doi.org/10.1038/nature04015

Kocharyan, G.G., 2016. Geomechanics of Faults. Moscow: GEOS. (in Russian)

Kocharyan, G.G., Novikov, V.A., Ostapchuk, A.A. & Pavlov, D.V., 2017. A study of different fault slip modes governed by the gouge material composition in laboratory experiments. Geophysical Journal International 208 (1), 521-528, doi: 10.1093/gji/ggw409.

Kocharyan, G.G., Markov, V.K., Ostapchuk, A.A. et al., 2014. Mesomechanics of shear resistance along a filled crack. Phys Mesomech 17, 123–133. https://doi.org/10.1134/S1029959914020040

Kocharyan, G.G., Ostapchuk, A.A. 2011. Variations in rupture zone stiffness during a seismic cycle. Dokl. Earth Sc. 441, 1591, https:// doi.org/10.1134/S1028334X11110250.

Kocharyan, G.G., Ostapchuk, A.A., Pavlov, D.V., Markov, V.K., 2018. The effects of weak dynamic pulses on the slip dynamics of a laboratory fault. Bulletin of the Seismological Society of America, 108(5B), 2983–2992. https://doi.org/10.1785/0120170363.

Kuksenko, V., Tomilin, N., Damaskinskaya, E. et al. 1996. A two-stage model of fracture of rocks. PAGEOPH 146, 253–263. https://doi.org/10.1007/BF00876492

Leeman, J., Saffer, D., Scuderi, M., et al., 2016. Laboratory observations of slow earthquakes and the spectrum of tectonic fault slip modes. Nat Commun 7, 11104, doi:10.1038/ncomms11104.

Lei, X., Li, S., Liu, L., 2018. Seismic b-value for foreshock AE events preceding repeated stick-slips of pre-cut faults in granite. Appl. Sci. 8, 2361. https://doi.org/10.3390/app8122361.

Lei, X. 2003. How does asperities fracture? An experimental study of unbroken asperities. Earth and Planetary Science Letters 213, 347-359, doi: 10.1016/S0012-821X(03)00328-5.

Lherminier, S., Planet, R., Levy dit Vehel, V. et al., 2019. Continuously Sheared Granular Matter Reproduces in Detail Seismicity Laws. Phys. Rev. Lett. 122, 218501, doi: 10.1103/PhysRevLett.122.218501.

Lippiello, E., Marzocchi, W., de Arcangelis, L. et al., 2012. Spatial organization of foreshocks as a tool to forecast large earthquakes. Sci Rep 2, 846, https://doi.org/10.1038/srep00846.

Mair, K., Frye, K.M., Marone, C., 2002. Influence of grain characteristics on the friction of granular shear zones. J. Geophys. Res. 107, 10, 2219. https://doi.org/10.1029/2001JB000516

Marone, C., 1998. Laboratory-derived friction laws and their application to seismic faulting. Annu. Rev. Earth. Planet. Sci. 26, 643-696. https://doi.org/10.1146/annurev.earth.26.1.643

Meng, L., Huang, H, Burgmann, R., et al., 2015. Dual megathrust slip behaviors of the 2014 Iquique earthquake sequence. Earth and Planetary Science Letters 411, 177-187. https://doi.org/10.1016/j.epsl.2014.11.041

Michel, S., Gualandi, A., Avouac, J.-P., 2019. Similarity scaling laws for earthquakes and Cascadia slow-slip events. Nature. 574, 522-526, doi: 10.1038/s41586-019-1673-6.

Michlmayr, G., Or, D., 2014. Mechanisms for acoustic emissions generation during granular shearing. Granular Matter 16, 627–640. https://doi.org/10.1007/s10035-014-0516-2

Molchan, G.M., 2003. Earthquake Prediction Strategies: A Theoretical Analysis. In: Keilis-Borok V.I., Soloviev A.A. (eds) Nonlinear Dynamics of the Lithosphere and Earthquake Prediction. Springer Series in Synergetics. Springer, Berlin, Heidelberg https://doi.org/10.1007/978-3-662-05298-3_5

Molchan., G., 2010. Space–Time Earthquake Prediction: The Error Diagrams. Pure Appl. Geophys. 167, 907–917, doi: 10.1007/s00024-010-0087-z.

Nielsen, S., 2017. From slow to fast faulting: recent challenges in earthquake fault mechanics. Phil. Trans. R. Soc. A 375, 20160016. http://dx.doi.org/10.1098/rsta.2016.0016

Nishitsuji, Y., Mori, J., 2014. Source parameters and radiation efficiency for intermediate-depth earthquakes in Northeast Japan, Geophysical Journal International 196, 2, 1247–1259, https://doi.org/10.1093/gji/ggt458.

Ostapchuk, A.A., Morozova, K.G., 2020. On the mechanism of laboratory earthquake nucleation highlighted by acoustic emission. Sci.Rep 10, 7245. https://doi.org/10.1038/s41598-020-64272-1.

Ostapchuk, A.A., Morozova, K.G. & Pavlov, D.V., 2019. Influence of the structure of a gouge-filled fault on the parameters of acoustic emission. Acta Acustica united with Acustica 105, 759–765, https://doi.org/10.3813/AAA.919356

Ostapchuk, A.A., Pavlov, D.V., Markov, V.K., Krasheninnikov, A.V. 2016. Study of acoustic emission signals during fracture shear deformation. Acoust. Phys. 62, 505-513, doi: 10.1134/S1063771016040138.

Ostapchuk, A.A., Pavlov, D.V., Ruzhich, V.V., et al. 2020. Seismic-acoustics of a block sliding along a fault. Pure Appl. Geophys. 117, 2641-2651. https://doi.org/10.1007/s00024-019-02375-1

Peng, Z., Gomberg, G., 2010. An integrated perspective of the continuum between earthquakes and slow-slip phenomena. Nat. Geosci. 3,599–607. doi: 10.1038/ngeo940.

Peng, H., Hattori, K., Zhuang, J., et al., 2017. Evaluation of ULF seismo-magnetic phenomena in Kakioka, Japan by using Molchan's error diagram. Geophysical Journal International 208, 1, 482–490. https://doi.org/10.1093/gji/ggw404

Rebetsky, Yu. L, Polets, A. Yu., & Zlobin, T. K., 2016. The state of stress in the Earth's crust along the northwestern flank of the Pacific seismic focal zone before the Tohoku earthquake of 11 March 2011. Tectonophysics, 685, 60–76. https://doi.org/10.1016/j.tecto.2016.07.016

Reber, J., Lavier, L., & Hayman, N., 2015. Experimental demonstration of a semi-brittle origin for crustal strain transients. Nature Geosci 8, 712–715. https://doi.org/10.1038/ngeo2496.

Ren, C.X., Dorostkar, O., Rouet-Leduc, B., et al., 2019. Machine learning reveals the state of intermittent frictional dynamics in a sheared granular fault. Geophysical Research Letters 46, 7395-7403, doi: 10.1029/2019GL082706.

Riviere, J., Lv Z., Johnson, P. & Marone, C. 2018. Evolution of b-value during the seismic cycle: Insights from laboratory experiments on simulated faults. Earth Planet. Sci. Lett. 482, 407-413, doi: 10.1016/j.epsl.2017.11.036.

Rosenau, M., Corbi, F. & Dominguez, S., 2017. Analogue earthquakes and seismic cycles: experimental modeling across timescales. Solid Earth 8, 597-635, doi: 10.5194/se-8-597-2017.

Saltykov, V.A., 2017. On the possibility of using the tidal modulation of seismic waves for forecasting earthquakes. Izv., Phys. Solid Earth 53, 250–261. https://doi.org/10.1134/S1069351317010128.

Scuderi, M. et al. 2016. Precursory changes in seismic velocity for the spectrum of earthquake failure modes. Nature Geosci. 9, 695–700, https://doi.org/10.1038/ngeo2775.

Scholz, C.H., 2002. The mechanics of earthquakes and faulting. Cambridge: Cambridge University Press.

Scuderi, M.M., Collettini, C., Vinti, C., Marone, C., 2017. Evolution of shear fabric in granular fault gouge from stable sliding to stick slip and implications for fault slip mode. Geology 45 (8), 731-734, doi: 10.1130/G39033.1.

Shebalin, P., Keilis-Borok, V., Gabrielov, A., Zaliapin, I., Turcotte, D., 2006. Short-term earthquake prediction by reverse analysis of lithosphere dynamics. Tectonophysics 413, 1-2, 63-75. https://doi.org/10.1016/j.tecto.2005.10.033.

Shiotani, T., Ohtsu, M., Ikeda, K., 2001. Detection and evaluation of AE waves due to rock deformation. Construction and Building Materials 15, 5–6, 235-246. https://doi.org/10.1016/S0950-0618(00)00073-8.

Shreedharan, S., Bolton, D.C., Riviere, J., et al., 2021. Competition between preslip and deviatoric stress modulates precursors for laboratory earthquakes. Earth and Planetary Science Letters 553, 116623. https://doi.org/10.1016/j.epsl.2020.116623

Trugman, D.T., Ross, Z.E., 2019. Pervasive foreshock activity across Southern Califirnia. Geophys. Res. Lett. 46, 8772-8781. https://doi.org/10.1029/2019GL083725.

Turcotte, D.L., 1999. Self-organized criticality. Rep. Prog. Phys. 62 1377 https://doi.org/10.1088/0034-4885/62/10/201.

Veedu, D.M., Barbor, S. 2016. The Parkfield tremors reveal slow and fast ruptures on the same asperity. Nature 532, 361–365. doi: 10.1038/nature17190.

Villegas-Lanza, J., Nocquet, J., Rolandone, F. et al., 2016. A mixed seismic–aseismic stress release episode in the Andean subduction zone. Nature Geosci 9, 150–154. https://doi.org/10.1038/ngeo2620.

Saffer, D., Wallace, L. 2015. The frictional, hydrologic, metamorphic and thermal habitat of shallow slow earthquakes. Nature Geosci 8, 594–600. https://doi.org/10.1038/ngeo2490

Zigone, D., Voisin, C., Larose, E., Renard, F., Campillo, M. 2011. Slip acceleration generates seismic tremor like signals in friction experiments. Geophys. Res. Lett. 38, L01315. https://doi.org/10.1029/2010GL045603

Zhuo, Y.-Q., Liu, P., Chen, S., et al., 2018. Laboratory observations of tremor-like events generated during preslip. Geophysical Research Letters 45 (14), doi: 10.1029/2018GL079201.

References from Supporting Information

Baruah S., Baruah S., Kalita A. , Biswas R., Gogoi N., Gautam J.L., Sanoujam M., Kayal J. R., 2012. Moment magnitude – local magnitude relationshipfor the earthquakes of the Shillong-Mikir plateau, Northeastern India Region: a new perspective,Geomatics. Natural Hazards and Risk, 3:4, 365-375. https://doi.org/10.1080/19475705.2011.596577

Bethmann F., Deichmann N., Mai P. M. , 2011. Scaling Relations of Local Magnitude versus Moment Magnitude for Sequences of Similar Earthquakes in Switzerland. 2011. Bulletin of the Seismological Society of America 101(2), 515-534. https://doi.org/10.1785/0120100179

Burgmann, R., 2018. The geophysics, geology and mechanics of slow fault slip. Earth and Planetary Science Letters 495, 112–134. https://doi.org/10.1016/j.epsl.2018.04.062

Hanks, T., Kanamori, H., 1979. A moment magnitude scale. J. Geophys. Res. 84, 2348–2350. https://doi.org/10.1029/JB084iB05p02348

Lei, X., 2003. How does asperities fracture? An experimental study of unbroken asperities. Earth and Planetary Science Letters 213, 347-359. https://doi.org/10.1016/S0012-821X(03)00328-5

Peng, Z., Gomberg, G., 2010. An integrated perspective of the continuum between earthquakes and slow-slip phenomena. Nat. Geosci. 3,599–607. doi: 10.1038/ngeo940.

Figure1.

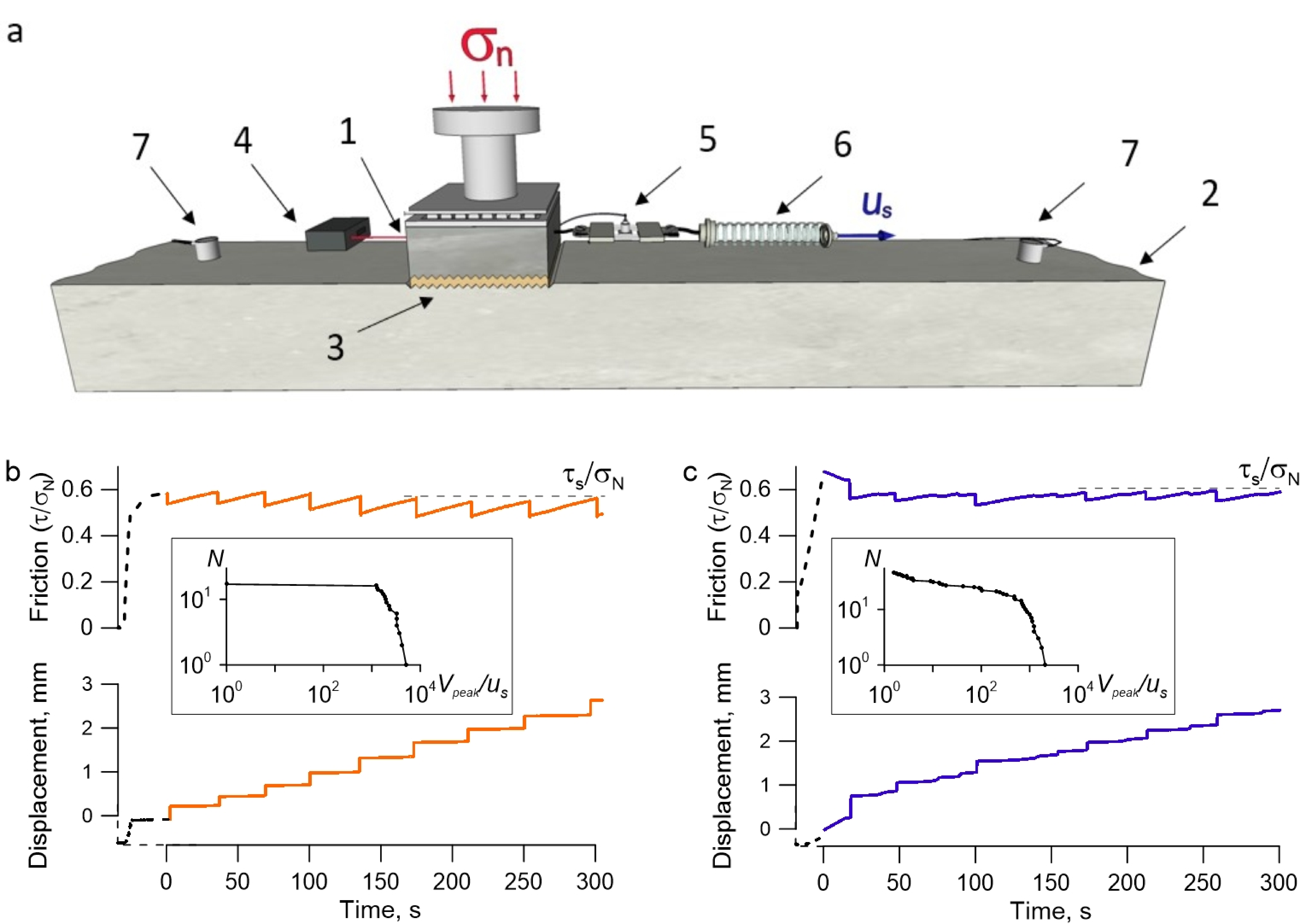

a
σ_n
u_s
1
2
3
4
5
6
7
7
b
c
Friction (τ/σ_N)
τ_s/σ_N
Displacement, mm
Time, s
N
V_{peak}/u_s

Figure2.

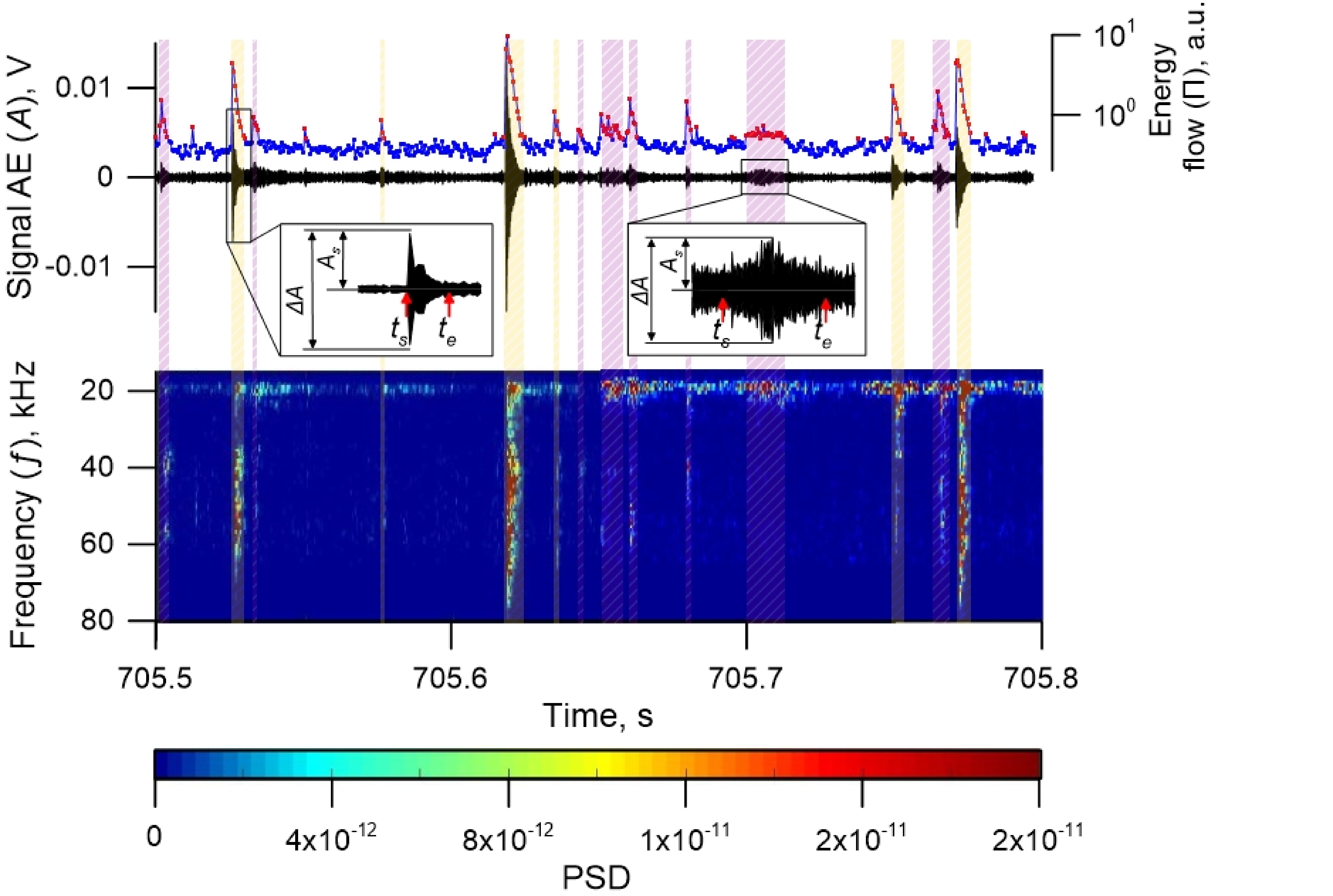

Signal AE (A), V
0.01
0
-0.01
Energy flow (Π), a.u.
10^1
10^0
ΔA
A_s
t_s
t_e
ΔA
A_s
t_s
t_e
Frequency (f), kHz
20
40
60
80
705.5
705.6
705.7
705.8
Time, s
0
4x10-12
8x10-12
1x10-11
2x10-11
2x10-11
PSD

Figure3.

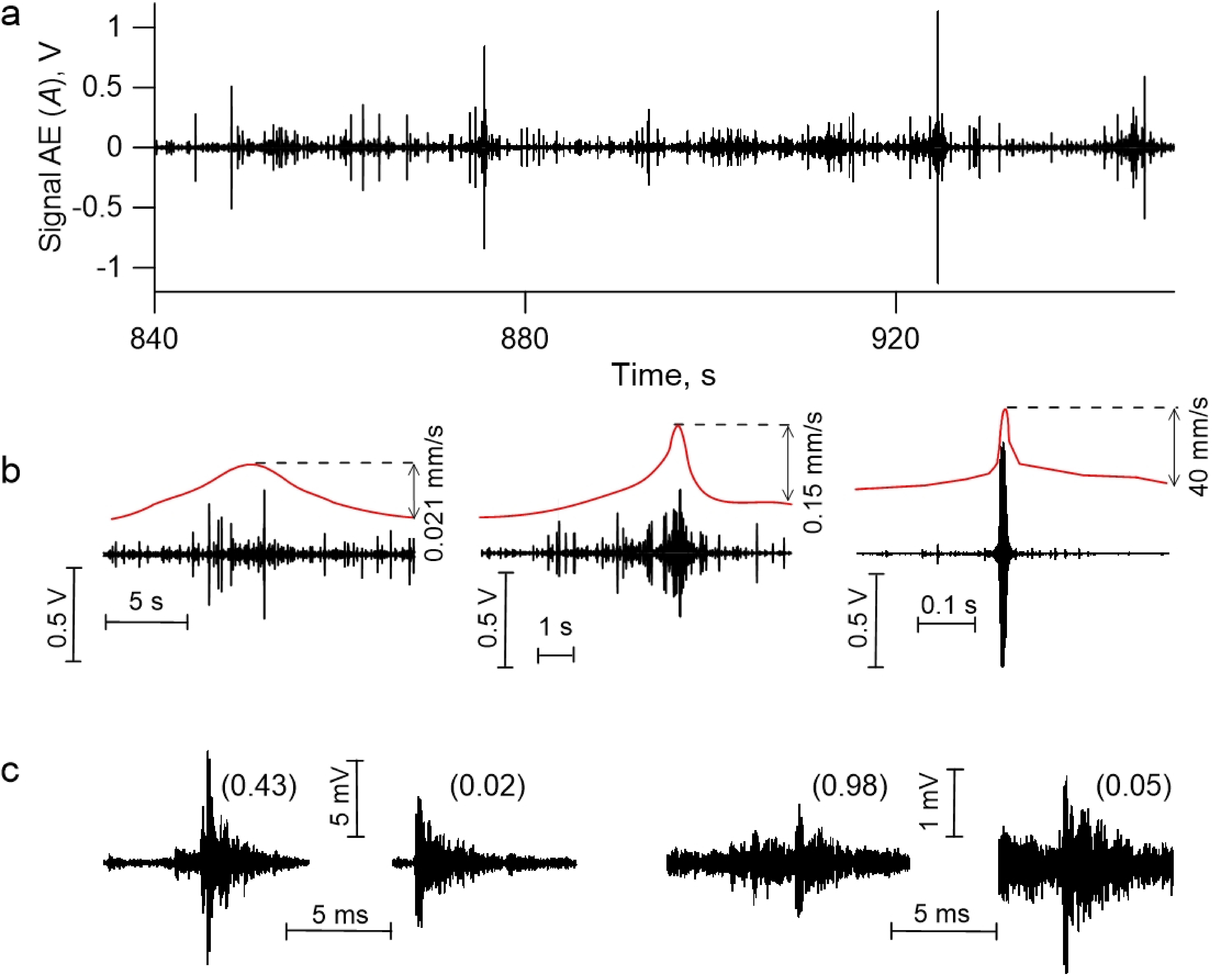
a
Signal AE (A), V
1
0.5
0
-0.5
-1
840
880
920
Time, s
b
0.021 mm/s
0.5 V
5 s
0.15 mm/s
0.5 V
1 s
40 mm/s
0.5 V
0.1 s
c
(0.43)
5 mV
(0.02)
5 ms
(0.98)
1 mV
(0.05)
5 ms

Figure4.

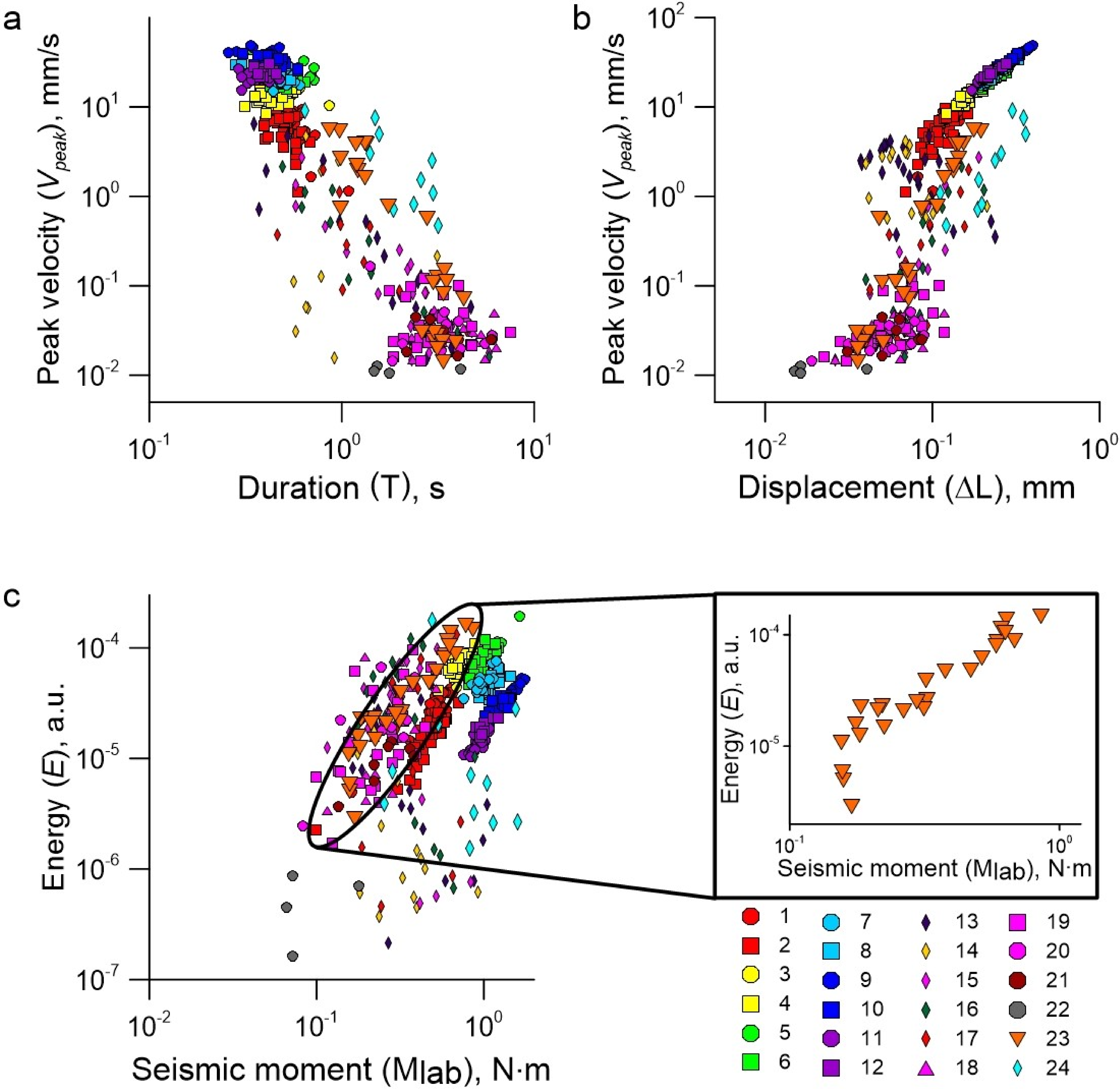
a
Peak velocity (V_{peak}), mm/s
Duration (T), s
b
Peak velocity (V_{peak}), mm/s
Displacement (ΔL), mm
c
Energy (E), a.u.
Seismic moment (M_{lab}), N·m
Energy (E), a.u.
Seismic moment (M_{lab}), N·m
1
2
3
4
5
6
7
8
9
10
11
12
13
14
15
16
17
18
19
20
21
22
23
24

Figure5.

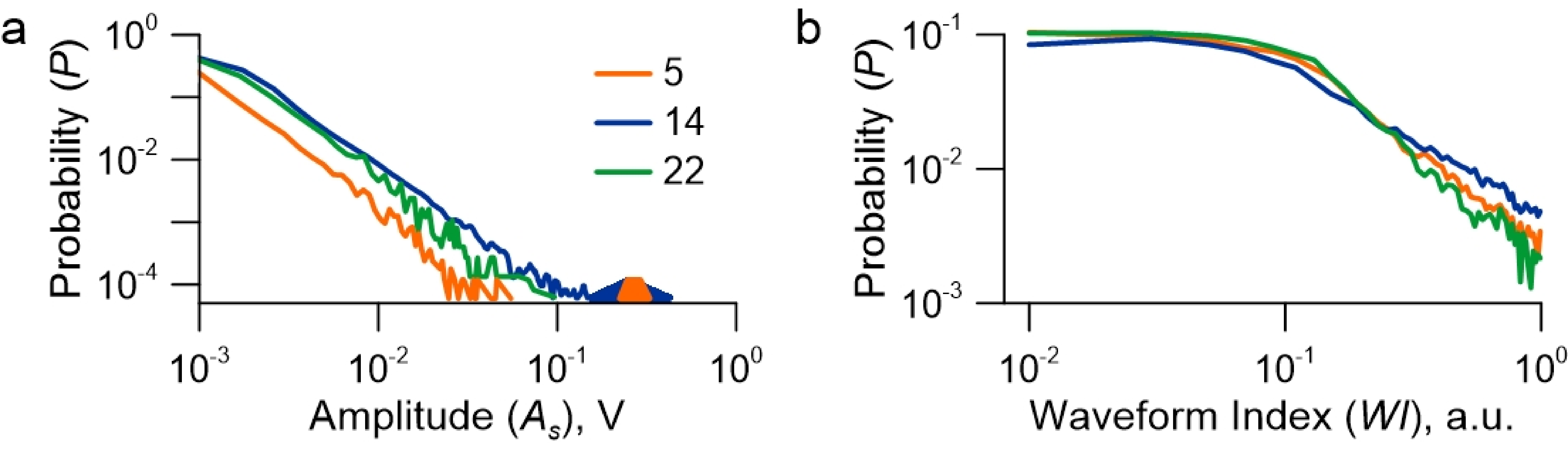

a
b
Probability (P)
Amplitude (A_s), V
Waveform Index (WI), a.u.
5
14
22
10^0
10^{-2}
10^{-4}
10^{-3}
10^{-1}

Figure6.

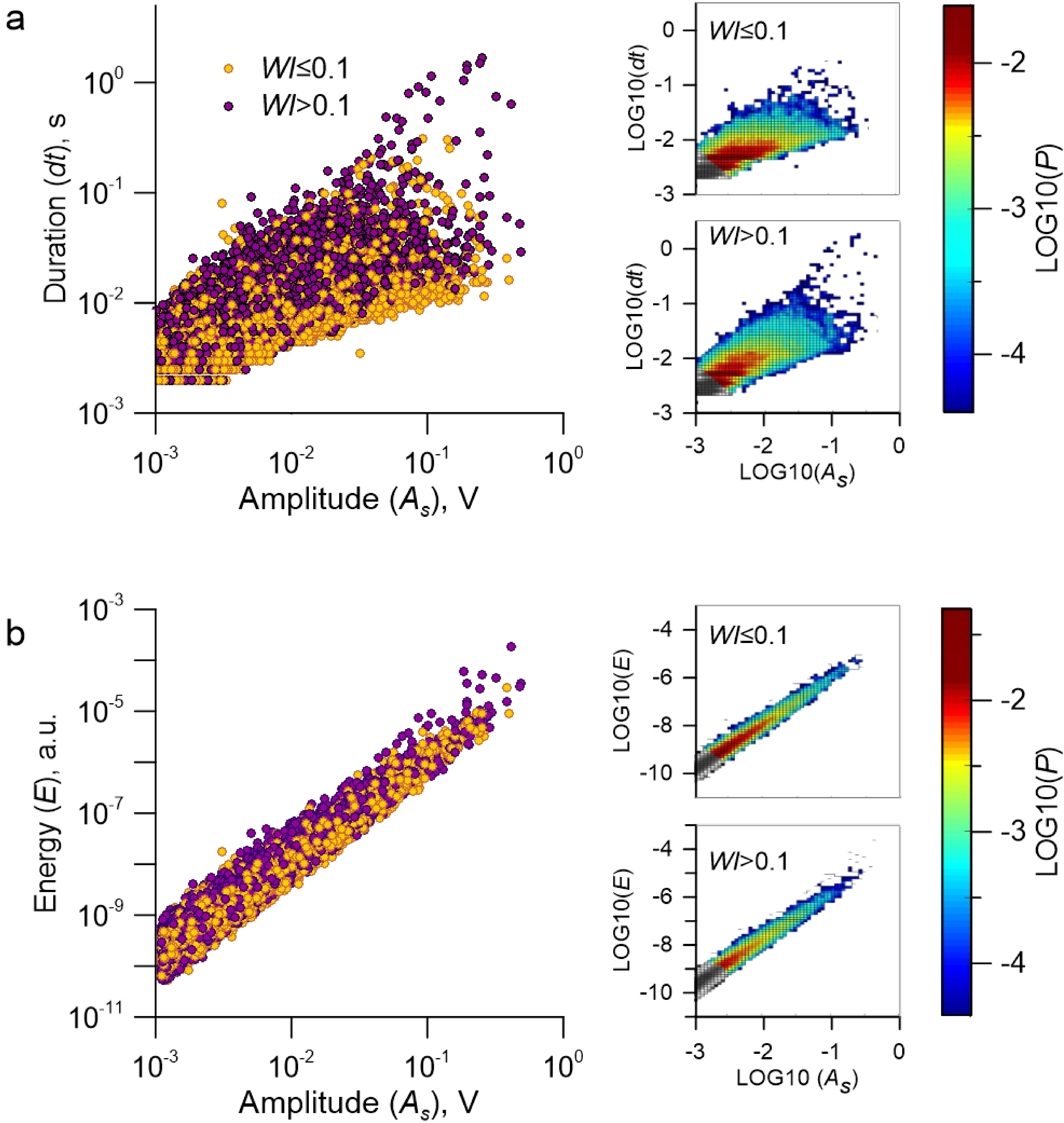
a
Duration (dt), s
Amplitude (A_s), V
WI≤0.1
WI>0.1
LOG10(dt)
LOG10(A_s)
LOG10(P)
b
Energy (E), a.u.
Amplitude (A_s), V
LOG10(E)
LOG10 (A_s)
LOG10(P)

Figure7.

a
b
Velocity, mm/s
Amplitude (A_s), V
AE rate, s^{-1}
Time, s
b-value
WI≤0.1
WI>0.1
Probability (P)
N
Amplitude (A_s), V

Figure8.

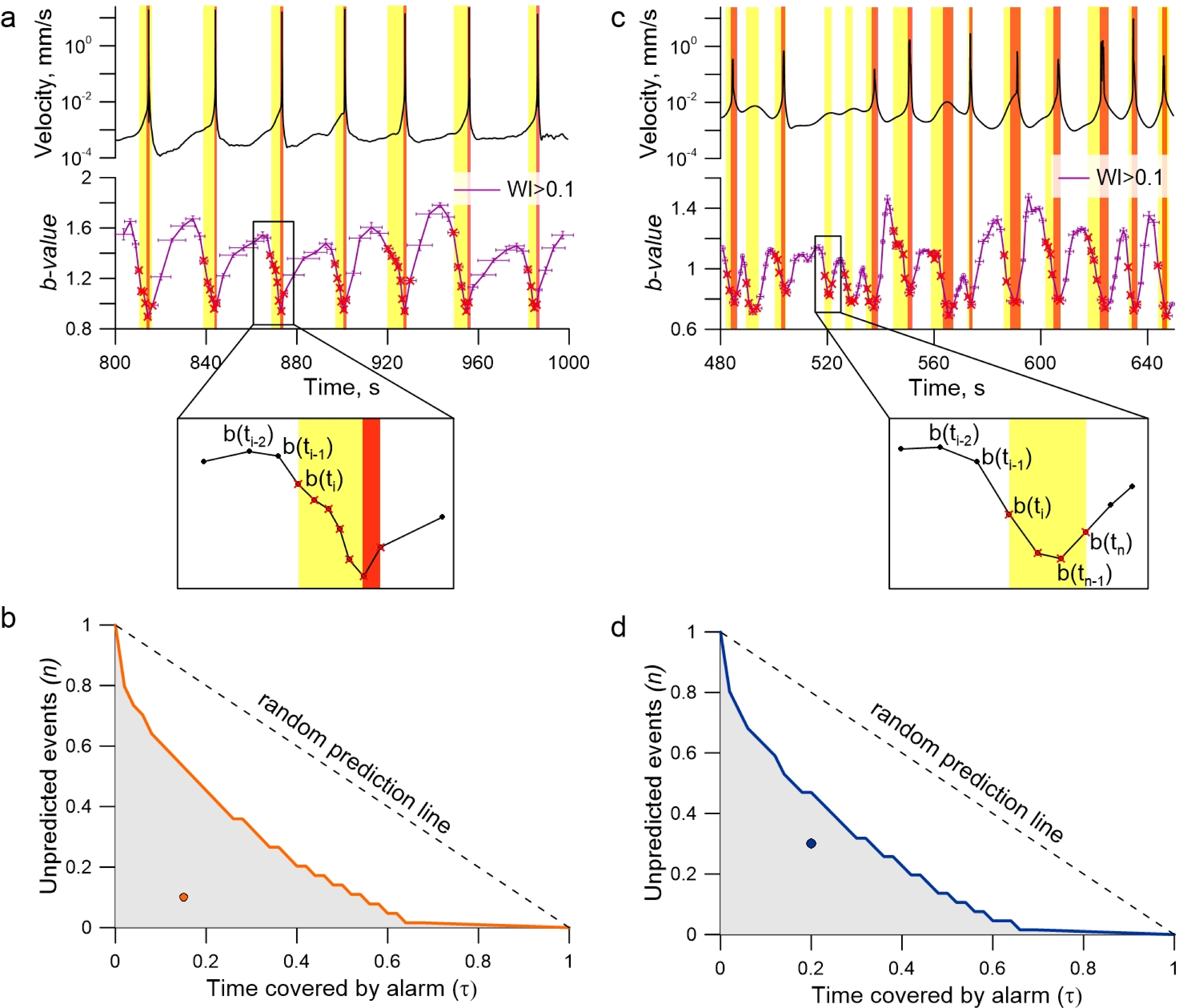

a
Velocity, mm/s
b-value
WI>0.1
Time, s
b(ti-2)
b(ti-1)
b(ti)
c
b(tn)
b(tn-1)
b
Unpredicted events (n)
Time covered by alarm (τ)
random prediction line
d